Suppression of precipitation bias on wind velocity from continuous-wave Doppler lidars

Liqin Jin, Jakob Mann, Nikolas Angelou, and Mikael Sjöholm

Department of Wind and Energy Systems, Technical University of Denmark, Frederiksborgvej 399, 4000 Roskilde, Denmark.

Correspondence: Liqin Jin (liqn@dtu.dk)

Abstract. In moderate to heavy precipitation, raindrops may deteriorate Doppler lidars' accuracy for measuring the line-of-sight wind velocity because their projected velocity on the beam direction differs greatly from that of air. Therefore, we propose a method for effectively suppressing the adverse effects of rain on velocity estimation by sampling the Doppler spectra faster than the raindrops' beam transit time. By using a special averaging procedure, we can suppress the strong rain signal by sampling the spectrum at 3 kHz. A proof-of-concept field measurement campaign was performed on a moderately rainy day with a maximum rain intensity of 4 mmh^{-1}, using three ground-based continuous-wave Doppler lidars at the Risø campus of the Technical University of Denmark. We demonstrate that the rain bias can effectively be removed by normalizing the noise-flattened 3-kHz-sampled Doppler spectra with their peak values before they are averaged down to 50 Hz prior to the determination of the speed. In comparison to the sonic anemometer measurements acquired at the same location, the wind velocity bias at 50 Hz (20 ms) temporal resolution is reduced from up to -1.58 ms^{-1} of the original raw lidar data to -0.18 ms^{-1} of the normalized lidar data after suppressing strong rain signals. This reduction of the bias occurs at the minute with the highest amount of rain when the focus distance of the lidar is 103.9 m with a corresponding probe length being 9.8 m. With the smallest probe length, 1.2 m, the rain-induced bias was only present at the period with the highest rain intensity and was also effectively eliminated with the procedure. Thus, the proposed method for reducing the impact of rain on continuous-wave Doppler lidar measurements of air velocity is promising, without requiring much computational effort.

1 Introduction

Precise determination of wind flow plays an important role in reducing loads on critical turbine components and power variations, correcting commonly used models for wind energy assessment, improving the performance of wind turbine controllers, and improving the prediction of the potential wind power extracted from the wind (Davoust et al., 2014; Jena and Rajendran, 2015; Li et al., 2018; Samadianfard et al., 2020; Guo et al., 2022). Besides, wind velocity estimation is also useful for understanding important phenomena, i.e., atmospheric boundary layer flows and wind turbulence (Van Ulden and Holtslag, 1985; Türk and Emeis, 2010; Debnath et al., 2017). Therefore, accurate measurements of wind velocity are crucial for many applications in meteorology and wind energy.

There are several available instruments capable of measuring wind speed, wind direction, and turbulence in wind energy, each with advantages and disadvantages. In-situ cup and sonic anemometers installed on meteorological masts (met masts) can

provide only point measurements of wind velocity (Izumi and Barad, 1970). On the contrary, Doppler lidars can accurately and remotely sense wind velocity by measuring Doppler spectra albeit with their limited ability to measure turbulence due to probe-length averaging effects (Sathe and Mann, 2013). For more than a decade, Doppler lidars have been widely used as a more and more reliable, valuable, and active optical remote sensing instrument with easier and cost-effective deployment. They

30 have been applied to estimate wind resource both onshore (Bingöl et al., 2009) and offshore (Sempreviva et al., 2008; Peña et al., 2009; Viselli et al., 2019; Elshafei et al., 2021), both by scanning lidars and profiling lidars (Mann et al., 2017; Menke et al., 2020; Gottschall et al., 2021) with good spatial and temporal resolutions (Henderson et al., 1991; Aoki et al., 2016).

Apart from the aforementioned, Doppler lidars have the potential of reducing loads on the turbine blade and tower through lidar prevision of the incoming gusts and flow (Bossanyi et al., 2014; Bos et al., 2016), and improving wind turbine control

35 (Mikkelsen et al., 2013; Schlipf et al., 2015; Zhang and Yang, 2020). Doppler lidars can also be applied to study atmospheric turbulence along the span of a suspension bridge (Cheynet et al., 2016) and study the turbulent wind field in the near-wake region of a tree (Angelou et al., 2022). In order to improve the measurement accuracy by lidars, Wildmann et al. (2020) reduced the volume-averaging effect on the retrieval of the wind flow statistics with ground-based Doppler lidars (see also Sathe and Mann, 2013). Brinkmeyer (2015) suggested the low coherence Doppler lidar approach using a pseudo-random broadband laser

40 source to obtain an effectively smaller sampling volume. It is self-evident that the precise determination of the wind velocity with Doppler lidars is paramount for many applications in wind energy.

Doppler lidars' measurements of wind velocity can be influenced by heavy rainfall because the projected velocity of raindrops on the propagation direction of the lidar beam will be different from the line-of-sight wind velocity. A synergy approach was proposed by Träumner et al. (2010), which combined radar and vertically scanning lidar measurements to estimate the

45 vertical wind velocity and the raindrop size distribution during rain episodes. Later, by using a velocity-azimuth display (VAD) scanning technique, wind speed, and rainfall speed were simultaneously retrieved in Wei et al. (2019), by fitting the two-peak spectrum with a two-component Gaussian model. The spectral peak close to 0 $\mathrm{ms^{-1}}$ is the Doppler signal of the vertical wind speed, which can be easily recognized in this scenario. Aoki et al. (2016) and Wei et al. (2021) proposed an iterative deconvolution method to retrieve raindrop size distribution during rain by using a vertically pointing coherent Doppler lidar.

50 However, for Doppler lidars which are not vertically pointing, the line-of-sight wind velocity is not close to zero and it is difficult to distinguish which part of the signal originated from raindrops or from air-following aerosols. Therefore, the purpose of the present study is to provide a proof-of-concept experimental investigation of a method we propose to suppress the precipitation signal from the aerosol signals, in order to reduce the rain-induced bias on the velocity estimation.

A field measurement campaign was carried out at Risø where three coherent continuous-wave (CW) Doppler lidars (Mikkelsen

55 et al., 2017) were deployed to point towards a common focus point very close to a mast-mounted sonic anemometer at 31 m height. Each lidar had different elevation angles, focus distances, and probe lengths. Therefore, it was possible to investigate the influence of these parameters on the performance of the post-processing method. The basic idea is to sample Doppler spectra rapidly, i.e. 3 kHz, which allows us to detect when a raindrop is in the beam. Measurements of a sonic anemometer are used as a reference to compare with the estimated line-of-sight wind velocity by the three lidars, before and after suppressing rain

Doppler signals in the Doppler spectra. The corresponding rain characteristics are retrieved from a ground-based disdrometer (Tilg et al., 2020) near the meteorological mast.

Section 2 introduces the field campaign and elaborately describes the instruments used. In Section 3, the measurement results of the sonic anemometers and the disdrometer are presented. The principle of Doppler spectral processing to retrieve the line-of-sight wind velocity as well as the method we propose to suppress strong rain signals are presented in detail in Section 4. Section 5 shows the comparison of 50 Hz and 1-minute wind velocity time series between the lidar and sonic anemometer measurements, with and without suppressing rain signals. The most important findings of our study are summarized in the Conclusion (Section 6).

2 Instrumentation

2.1 The WindScanner system

In order to validate the method to reduce the influence of the precipitation on the estimated wind velocity, we conducted a field experiment at the Risø campus of the Technical University of Denmark (DTU), as shown in Fig. 2. The surrounding terrain is flat and agricultural. The short-range WindScanner system with three CW Doppler lidars (Fig. 1) which are developed by DTU Wind and Energy Systems, was used to measure the wind field (Vasiljević et al., 2017; Mikkelsen et al., 2020). The three lidars employ a dual-prism beam scanner, enabling them to orient the beam in any direction within $\pm 61°$ of the adjustable center axis (Sjöholm et al., 2014; Mikkelsen et al., 2008). The direction of the line-of-sight of each lidar is steered by two prism motors and a focus motor controls the measurement location along the beam for these lidars. For this campaign, the sampling frequency of spectra is set to be 3 kHz. A central master computer is used to synchronize the short-range wind lidars to scan the same pattern in space simultaneously, however, all three lidars are focused on one static point in this investigation.

The three ground-based lidars were staring at a point 1 m north of a sonic anemometer (USA-1, METEK) which was located 31 m above the ground. The lidar heads were covered with green rain barrels to avoid raindrops covering the windows of the lidars (Fig. 1). The intention of using three lidars is to investigate the influence of different probe lengths and different elevation angles on the performance of the method to suppress rain signals. The full-width-at-half-maximum (FWHM) of the Lorentzian weighting function or the probe length can be approximated as (Sathe and Mann, 2013),

$$\text{FWHM} = 2 \cdot z_R = 2 \cdot \frac{\lambda \cdot r^2}{\pi a_0^2} \tag{1}$$

where z_R is the Rayleigh length, defined as the distance from the focus point to where the cross-sectional area of the laser beam is doubled (Angelou et al., 2012b), r is the distance from the lidar to where the beam is focused, λ is the laser wavelength, which is 1.565 μm, a_0 is the e^{-2} intensity radius of the laser beam at the lidar telescope, which is about 33 mm. A list of the measurement parameters of the three lidars is summarized in Table 1 and the three-dimensional view of the three lidars' configuration is depicted in Fig. 2. Lidar #1 is placed on a slope, therefore it has a relatively bigger elevation angle of about 58°, but has the smallest probe length of 1.2 m, compared with lidar #2 and #3. The measurement period of the three lidars is from 15:12 to 23:29 (UTC+1) on September 27th, 2022. All times mentioned in the paper are UTC+1.
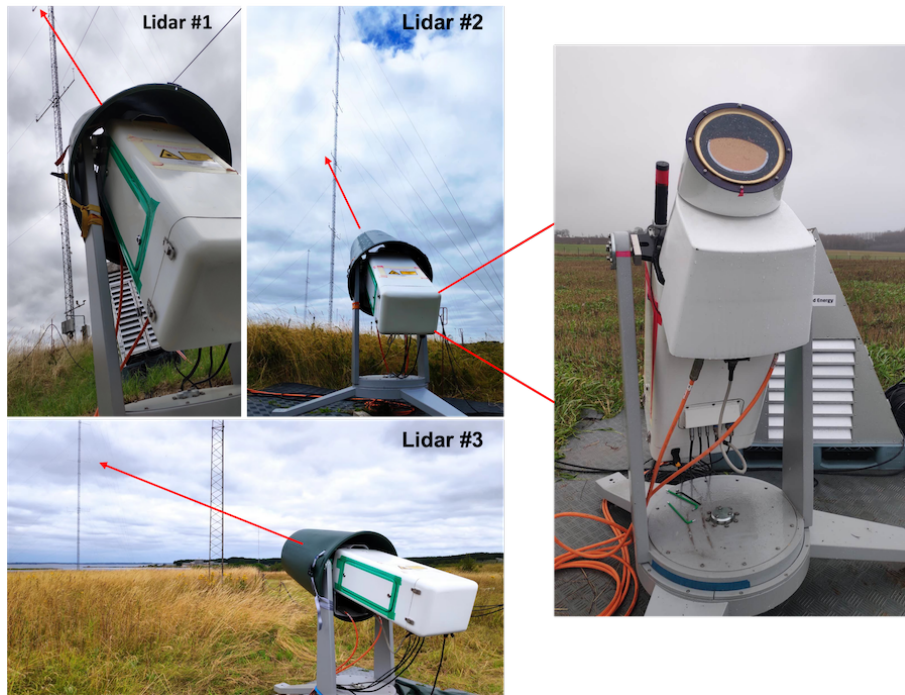
Figure 1. Three CW lidars pointed at a common focus point close to a sonic anemometer on a met mast at DTU Risø campus.
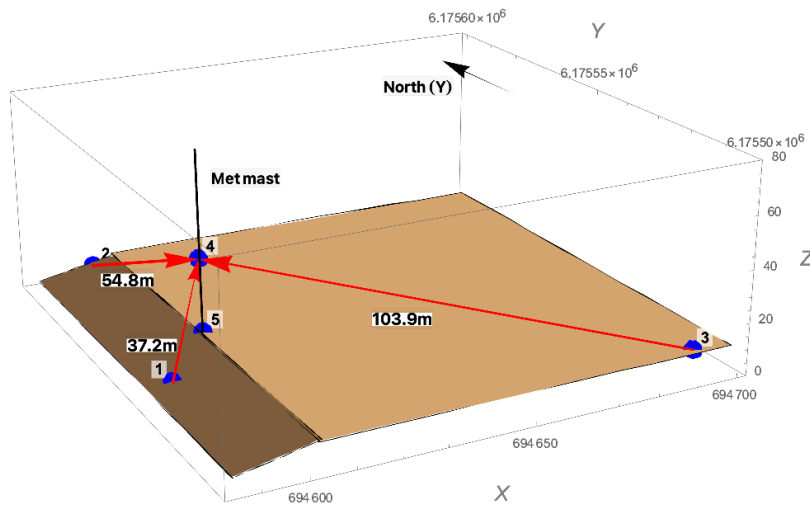
Figure 2. Experiment setup at DTU Risø campus in the three-dimensional view. Blue points marked by 1, 2, and 3 are the three CW Doppler lidars, focused at the common point 4 which is 1 m north of the sonic anemometer at a height of 31 m above the ground. Point 5 is the base of the met mast. The black solid line indicates the met mast.

Table 1. Summary of the measurement parameters of the three CW lidars. Note geographic beam direction is relative to the North and clockwise positive.

	Elevation angle α (°)	Rayleigh length z_R (m)	Line-of-sight focus distance r (m)	Geographic beam direction (°)
Lidar #1	57.9	0.6	37.2	42.6
Lidar #2	34.6	1.4	54.8	172.9
Lidar #3	15.3	4.9	103.9	299.3

The backscattered light mixed and amplified by the local oscillator is sampled at a rate of 120 MHz and Doppler spectra containing 512 frequency bins are calculated by Fast Fourier Transform (FFT) with a frequency resolution of $(120\,\text{MHz})/512 = 234.4\,\text{kHz}$. The wind speed resolution is calculated from this frequency resolution and the laser wavelength λ, yielding $(1.565\,\mu\text{m}/2)\cdot(234.4\,\text{kHz}) = 0.183\,\text{ms}^{-1}$. In order to determine the sign of line-of-sight velocities, the in-phase/quadrature-phase (IQ) detection method (Abari et al., 2014) is employed, which mixes the received signal with two local oscillator signals phase shifted by 90° relative to each other. Subsequently, a block averaging of 78 spectra results in a final sampling period of $512 \cdot 78\,/(120\,\text{MHz}) = 0.33\,\text{ms}$, corresponding to a spectrum rate of 3 kHz. Therefore, at every minute each lidar will provide 180000 spectra. Additionally, Bartlett's method is used to obtain the power spectral density (PSD) of each spectrum (Press et al., 1988, Chap. 13), which is the square of the absolute value of the FFT of the detector's time series. The median method (Held and Mann, 2018) is employed to determine wind velocity.

A raindrop's beam transit time t is defined as the time it takes for the raindrop to enter and exit the laser beam, which is calculated by dividing its falling path l by its downfall speed V_f, as follows:

$$t = \frac{l}{V_f} = \frac{2w(z)}{\cos(\alpha) \cdot V_f} \tag{2}$$

where $w(z)$ is the beam width at a position z (measured from the focus) along the beam and α is the elevation angle of the laser beam. In the case where $w(z)$ is the smallest and V_f is the largest, then the beam transit time will be the shortest. This occurs when a large raindrop falls through the laser beam's focus (position z_0 in Fig. 3a) with a maximum falling speed V_{fmax} of 9 ms^{-1} from the disdrometer measurement in Fig. 7b, which is

$$t_s = \frac{2w_0}{\cos(\alpha) \cdot V_{fmax}} \tag{3}$$

where $w_0 = \frac{r \cdot \lambda}{\pi \cdot a_0}$ is the beam waist and $a_0 = 33$ mm is the effective radius of the telescope. For lidar #1 with a beam waist of 0.56 mm and an elevation angle of 57.9°, the shortest beam transit time is 0.234 ms, while it is 0.362 ms for lidar #3 with a beam waist of 1.57 mm and an elevation angle of 15.3°. Most often, however, raindrops' transit time is longer than the aforementioned shortest time if their paths are away from the lidar focus (position z_1 in Fig. 3a) and if they fall slower than V_{fmax}. In this study, it is reasonable to set the spectral sampling frequency to 3 kHz so that the sampling period for a spectrum

(a)   (b)
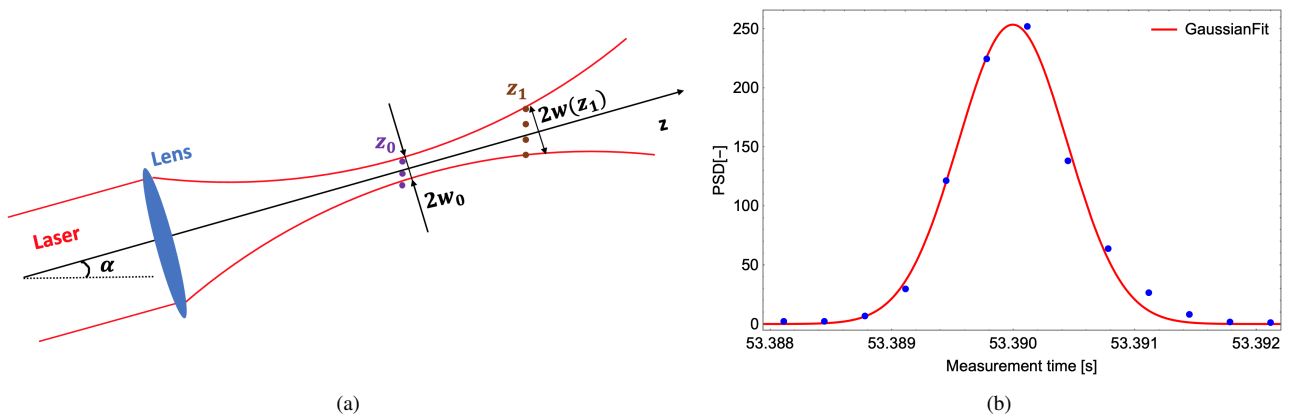
Figure 3. An illustration of raindrops falling through a focused laser beam. **(a)** Raindrops cross the laser beam at random positions z_0 and z_1, where z_0 is the focus point. **(b)** Raindrop-induced Doppler signal during a raindrop's passage through the beam follows a Gaussian distribution since the laser beam's transverse intensity profile is Gaussian (Harris et al., 2001; Jin et al., 2022).

115   (0.333 ms) is shorter than the beam transit of raindrops. Therefore, the rare instances where a raindrop resides in the beam can be identified (raindrop-induced Doppler signals detected in several successive spectra in Fig. 3b) and suppressed based on the lidar measurements.

2.2   METEK sonic anemometer

The meteorological mast location is approximately 120 m northwest of the DTU V52 wind turbine and its base is 7.3 m above
120   the sea surface (Fig. 2). There are five sonic anemometers (USA-1, Metek) on booms facing north and five cup anemometers (P2546A from WindSensor) on booms facing south, placed at 18 m, 31 m, 44 m, 57 m, and 70 m above the terrain (Fig. 4). The sampling frequency of the sonic anemometers was 50 Hz. Furthermore, the mast is instrumented with a vector wind vane (W200P from Kintech Engineering) at 41 m, and two air temperature sensors (Pt 100, developed by DTU) mounted at 18 m and 70 m, respectively. In order to test the consistency of the mast wind measurements, the available sonic and cup observations
125   at different heights are compared in the following section. The sonic anemometer at 31 m is used as a reference for further comparison with the radial wind velocity detected by the three lidars.

In this step, it is also important to get accurate orientation of the sonic anemometer. For this purpose, the azimuth angle of the boom is considered as the direction offset of the sonic anemometer relative to the North. Here the Leica Total Station (Fig. 4b) was used to scan the sonic anemometer at 31 m height, the boom at the same height, and the three lidars. The scanned
130   results of the sonic anemometer at 31 m high are presented in Fig. 4c and the azimuth angle of the boom to the north is $13.2°$ in the UTM32 zone and the tilt angle of the sonic to the vertical is $1.9°$, which will be used to derive the unit vectors when projecting the reference sonic velocity onto the directions of the three lidar beams. Consequently, the unit vectors of three lidar beams are $[-0.36, -0.39, -0.85]$, $[-0.10, +0.82, -0.57]$ and $[+0.84, -0.47, -0.26]$, respectively.

(a)

(b)

(c)
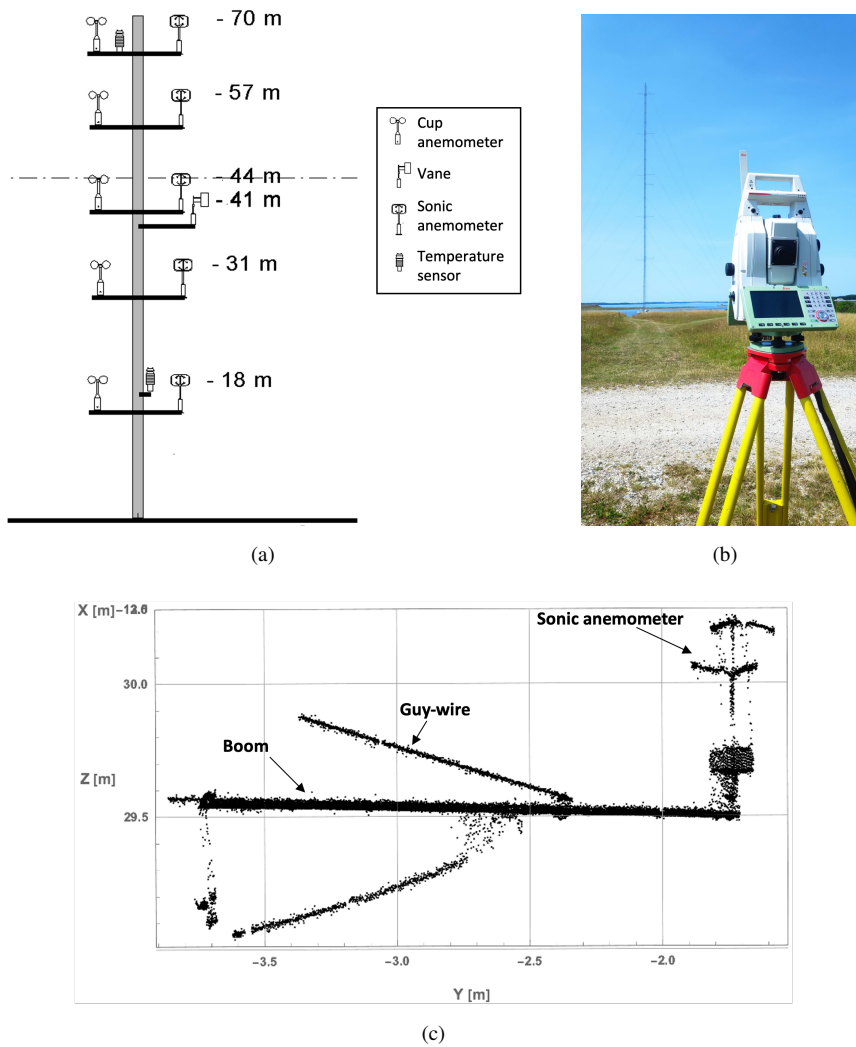
Figure 4. Orientation calibration of sonic anemometers on the met mast. **(a)** A sketch of the V52 meteorological mast with the instrumentation. The dashed line indicates the hub height of the DTU V52 wind turbine. **(b)** Leica Total Station (Leica Geosystems, last access: 12 March 2023.). **(c)** Scanned cloud points of the sonic anemometer at the height of 31 m.

Figure 5. Thies Laser Precipitation Monitor (LPM) at DTU Risø campus.

2.3 Disdrometer measurements

135 The falling velocity and diameter of the raindrops were measured by a laser optical disdrometer manufactured by Thies (Laser Precipitation Monitor, LPM), with a transmitter head emitting a horizontal laser-light plane and a receiver head detecting the emitted laser light (Fig. 5). When a raindrop intersects the laser beam, it attenuates the power of the transmitted laser light with a specific magnitude as a function of the falling velocity and the diameter. After the application of a proprietary algorithm, the measured raindrops are classified into specific velocity and diameter classes, which are outputted with a temporal resolution

140 of 1 minute. Here, raindrops' diameter is given as the equi-volume sphere diameter (Angulo-Martínez et al., 2018). Some technical details of Thies LPM disdrometer are given in Table 2. This disdrometer was about 20 m north of the met mast.

3 Sonic anemometer and disdrometer data

3.1 10-minute averaged sonic data

Before analyzing the sonic and lidar data, the sonic and cup wind speed as well as the sonic and vane wind direction at different

145 heights were compared. In Fig. 6 a and b we show that the 10-minute averaged wind speeds by sonic and cup anemometers are in good agreement for all heights including the height of 31 m where the lidars were measuring. The slope of a linear regression is 1.008 with a coefficient of determination R^2 equal to 0.997, which shows that wind speeds measured by the sonic anemometers agree well with that measured by cup anemometers (with only a 1% difference). The same conclusion can be

Table 2. Technical details of the Thies Laser Precipitation Monitor (LPM) (Clima, T, last access: 2 June 2023.).

	Thies LPM
Laser wavelength [nm]	786
Size of laser-light plane [mm^2]	4560
Number of diameter classes	22
Min of diameter classes [mm]	0.1875
Number of velocity classes	20
Min/max of velocity classes [ms^{-1}]	0.1/15

drawn for the wind direction in Fig. 6 c and d. Besides, the mean absolute difference of wind speed between the sonic and cup anemometer at 31 m height is 0.11 ms^{-1} and that for wind direction between the sonic at 44 m and the vane at 41 m height is $1°$. However, for further comparison with the lidar data, the three unit vectors describing the direction of the line-of-sight are used to project the wind vector measured by the sonic anemometer onto the lidar's line-of-sight, as mentioned in Sect. 2.2.

The experiment started at 15:12 (UTC+1) and stopped after three-hour measurements. This is because the measurement volumes came into the wake of the Vestas V52 wind turbine. Whether a turbine wake affects the measurements is unknown but we wanted to avoid this complication. From 15:12 to 18:11, marked by the two red vertical lines in Fig. 6, the 10-minute mean wind speed obtained from the sonic anemometer at 31 m is in the interval $[2.02$ ms^{-1}, 6.59 ms$^{-1}]$, while the wind direction is in the interval $[110.9°, 164.8°]$.

3.2   1-minute disdrometer data

The 1-minute averaged rain intensity from 15:00 to 19:30 (UTC+1) measured by the Thies disdrometer is shown in Fig. 7a. It started to rain at 15:15, reached the highest precipitation rate of about 4 mmh^{-1} at 15:48, and stopped after 19:00. Moderate rain is defined as a precipitation rate between 2.6 mm and 7.6 mm per hour (Glossary of Meteorology (June 2000), last access: 21 June 2023.). The selected comparison period from 15:12 to 18:11 includes no-rain, light-rain (the precipitation rate is smaller than 2.5 mmh^{-1}), and moderate-rain minutes, which enables the investigation of the performance of the method we propose to suppress rain signals during precipitation levels. During the highest rain intensity period, most of the raindrops have mass-weighted mean diameters smaller than 2 mm and the falling velocity smaller than 6 ms^{-1} as shown in Fig. 7b.
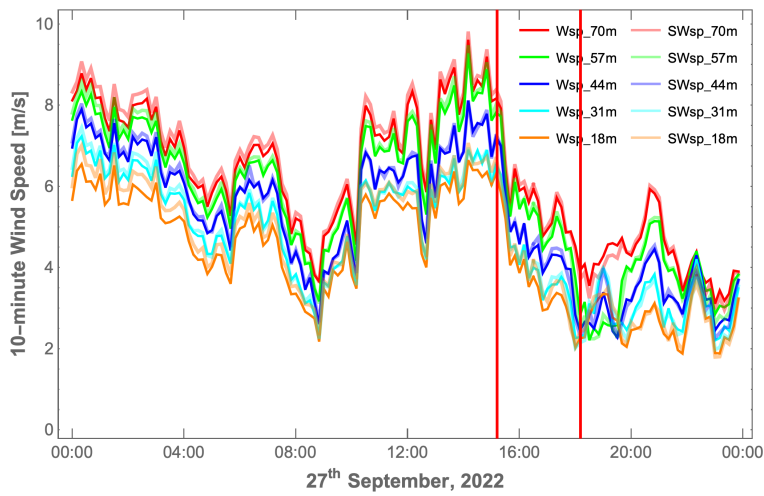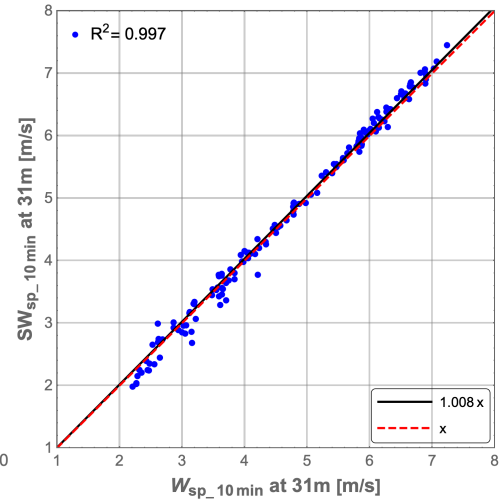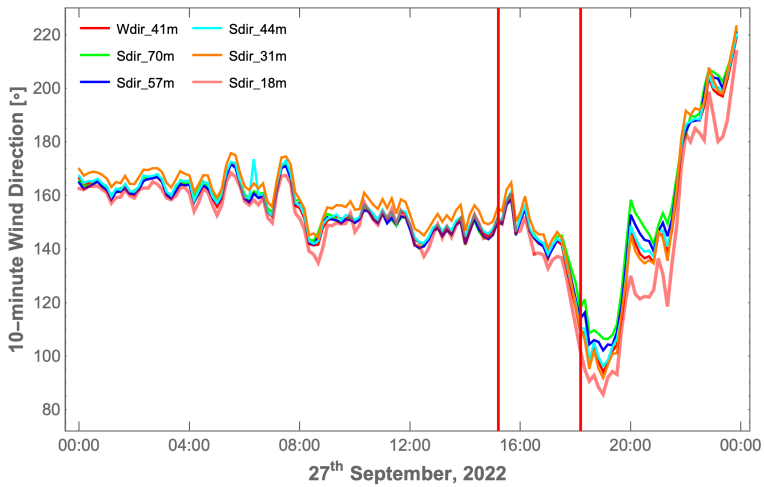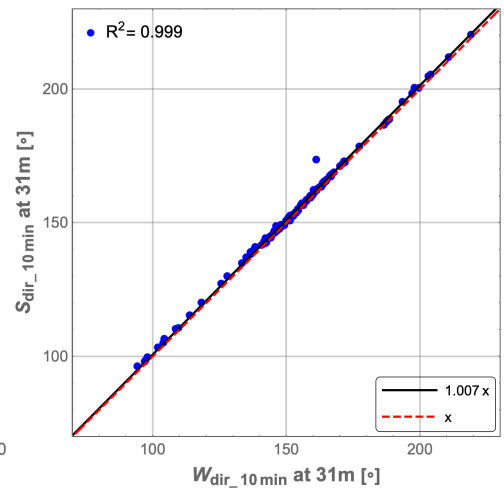
Figure 6. Comparison of 10-minute wind measurements with the wind vane, sonic, and cup anemometers at several vertical heights. **(a)** 10-minute wind speed by sonic (SW_{sp}) and cup (W_{sp}) anemometers. **(b)** 10-minute wind direction by sonic anemometers (S_{dir}) and the wind vane (W_{dir}). **(c)** and **(d)** Linear regression of 10-minute wind speed and direction. The two red lines mark the comparison period of lidar and sonic data from 15:12 to 18:11 (UTC+1).
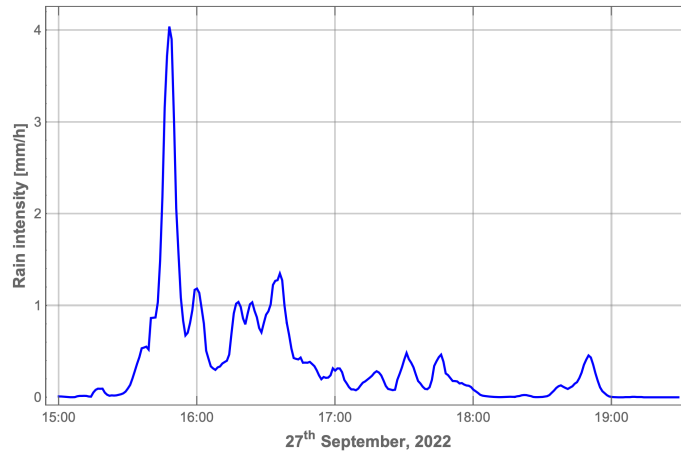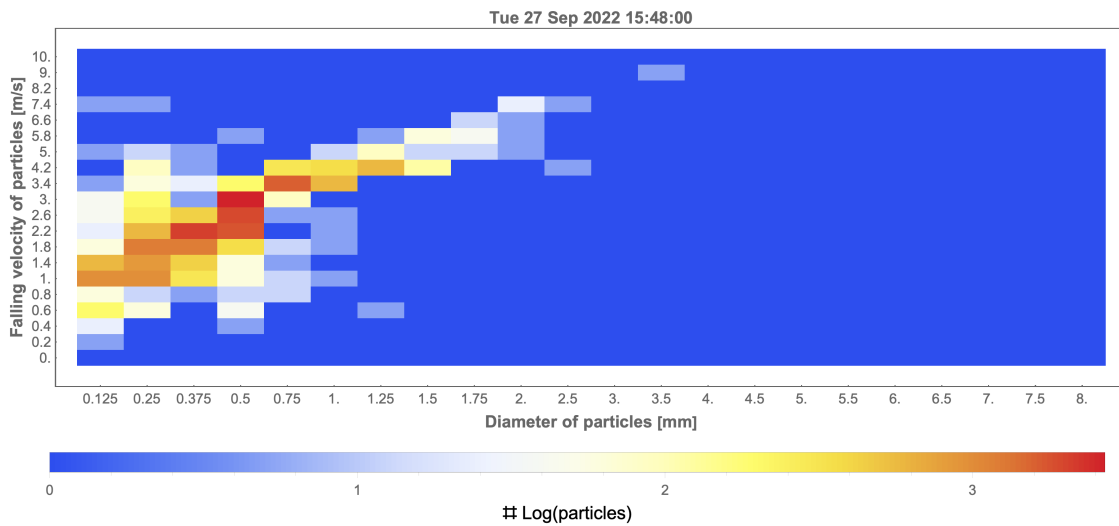
Figure 7. Rain event from 15:00 to 19:30 (UTC+1) on September 27th, 2022 measured by the Thies Laser Precipitation Monitor disdrometer. **(a)** 1-minute Rain intensity. **(b)** Distribution of the number of measurements with specific vertical falling speeds and mass-weighted mean diameters at the minute (15:48) with the highest rain intensity (color-coded).
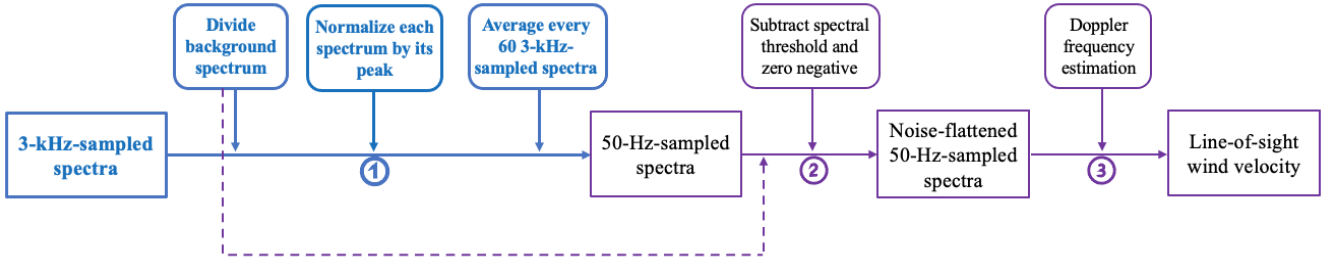
Figure 8. Processing block diagram of the rain-suppressing normalization method (the solid lines from ① to ③) to estimate wind velocity based on 3-kHz-sampled Doppler spectra. The processing block diagram of Doppler spectra at lower frequencies that do not resolve individual raindrops (like 50 Hz) reduces to just the purple path including the "Divide background spectrum" block (dashed purple line before label ②).

4 Suppression method of the rain bias

4.1 Lidar data processing

Doppler spectra are usually averaged to lower frequencies, ranging from 50 Hz to a few hundred Hertz. A 50-Hz-sampled spectrum can be processed by the following steps (the purple path marked by ② and ③ in Fig. 8 along with the dashed purple line): the spectrum is divided by the background spectrum and subtracted by its spectral threshold to flatten background noise. Consequently, the line-of-sight velocity is retrieved based on this noise-flattened 50 Hz spectrum after applying Doppler frequency estimation methods (Peña et al., 2015, Chap. 5).

However, from a random 3 kHz spectrum acquired during a minute (15:48, UTC+1) with moderate-rain precipitation, it is obvious that sometimes the spectrum has a very high, narrow peak as shown in Fig. 9b. This is caused by a raindrop falling through the beam, the intensity of which should be compared to the ones of the more commonly occurring spectra where the Doppler signal is caused by the aerosols (Fig. 9a). Here the width of the Doppler spectrum in Fig. 9a is relatively wider because the aerosols within the measurement volume of the lidar have slightly different velocities and the peak value is much lower. In contrast, the spectrum caused by the raindrop is very narrow because of the single velocity of the drop. From the histogram of the maximum values of the spectra obtained during this moderate-rain minute (Fig. 9d), the very high back-scattering events marked by the red circle are the large raindrops passing through the center line of the laser beam close to the beam waist. These could potentially cause a bias between the radial wind velocity measured by the lidar and the sonic.

Therefore, based on the above observations, we propose the rain-suppressing normalization method to reduce the influence of rain on wind velocity estimation. The detailed process is indicated by the solid lines and marked by ① to ③ in Fig. 8, which is:

① every 3-kHz-sampled Doppler spectrum without suppressing rain signal (blue curve marked by "Raw" in Fig. 9a) is divided with the background spectrum (red curve in Fig. 9a) to flatten the noise floor. Then, the noise-flattened 3-
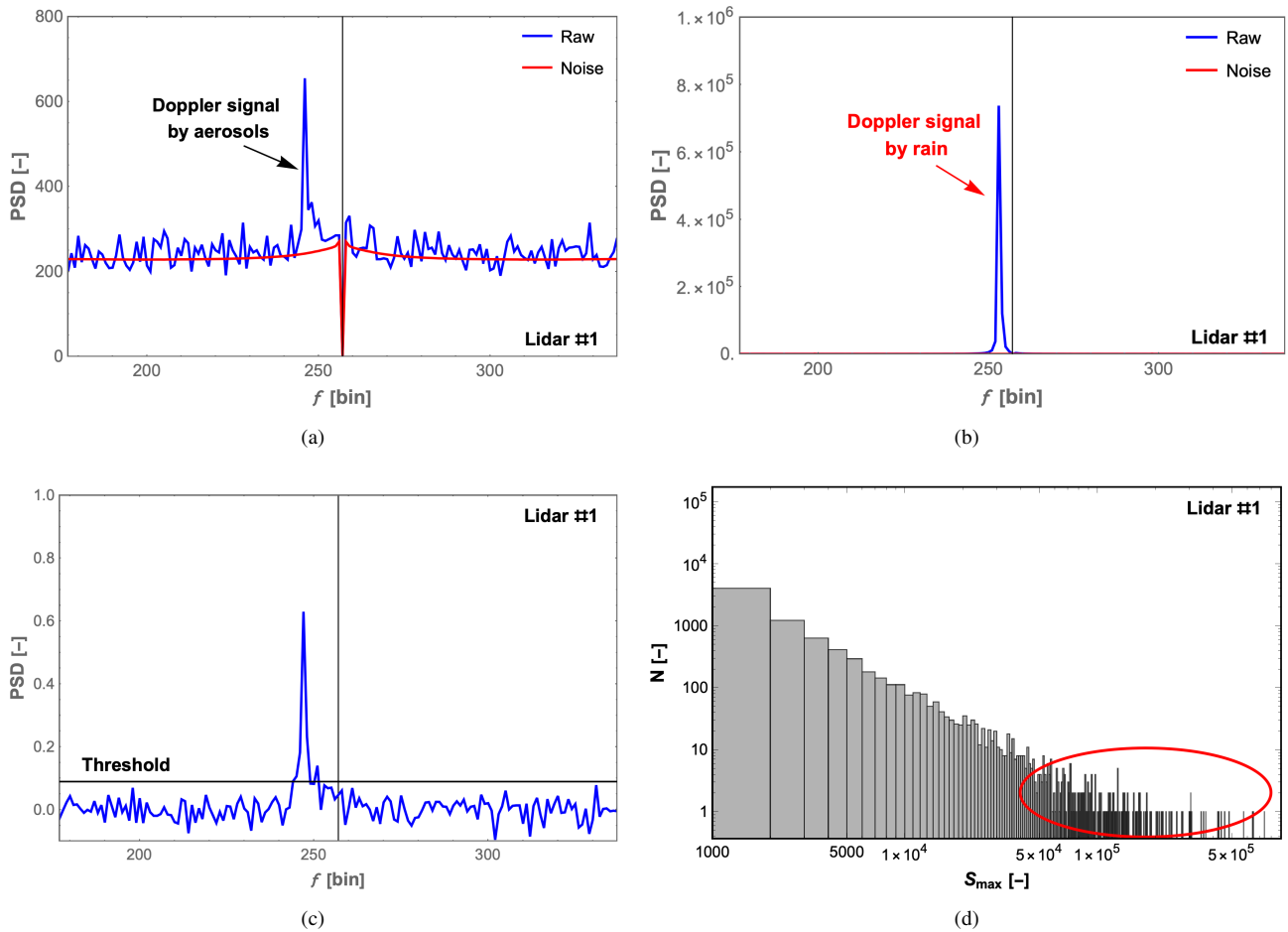
Figure 9. Examples of representative Doppler spectra measured at the moderate-rain minute (15:48, UTC+1) with the highest rain intensity. **(a)** A 3-kHz-sampled spectrum containing only wind signal (blue) and the mean background spectrum (red). **(b)** A 3-kHz-sampled spectrum containing rain signal (blue) and the mean background spectrum (red). **(c)** A noise-flattened 50-Hz-sampled spectrum and its spectral threshold. **(d)** Histogram of the maximum spectral energy S_{max} of 180000 raw spectra over the duration of the same minute with a red circle marking the strongest rain signals. The solid black line stands for the zero-Doppler shift at frequency bin 257.

kHz-sampled spectra are normalized by their own peak value. Subsequently, every 60 normalized spectra are averaged down to 50 Hz to achieve a better signal-to-noise ratio (Branlard et al., 2013) and ease the comparison with the sonic anemometer;

② a spectral threshold (black line in Fig. 9c) is subtracted from every 50 Hz spectrum and negative values are zeroed. The spectral threshold is calculated based on the mean value (μ) plus multiple numbers of the standard deviation (σ) of the power spectral density over a wind-signal-free Doppler frequency range;

③ the median method is used to determine line-of-sight velocity from the final 50 Hz spectra (Fig. 9c), as it has the least biases for weak signals (Angelou et al., 2012a) in comparison to the maximum and centroid methods (Held and Mann, 2018).

In the first step, the background spectrum is calculated as the median power spectral density per frequency of 180000 Doppler spectra, acquired during one minute. After that, we choose the smaller background for any pair of frequencies $(-f, f)$, which provides the true background noise even if the wind velocity is constant over the minute. However, this procedure will not work if the wind velocity is around zero, since the wind Doppler signal would be present on both sides of the zero frequency bin. Then, a real atmospheric Doppler signal would be included in the background spectrum rather than the real background noise. Therefore, in the case of lidar #1 where the line-of-sight velocity fluctuates around zero (the vertical line at frequency bin 257 corresponding to the zero-Doppler shift in Fig. 9), a background spectrum is calculated for a period where the line-of-sight speed is away from zero.

After obtaining 50 Hz spectra in the third step, it is vital to determine a correct spectral threshold to define the signal caused by the wind in a Doppler spectrum. This is because a too-high spectral threshold would result in the unexpected removal of the useful Doppler signal and cause false 0 ms^{-1} wind velocity, while a too-low spectral threshold would leave a lot of noise in the spectrum, deteriorating the accuracy of the wind velocity estimation. As concluded in Angelou et al. (2012a), the optimum number of standard deviations to define the threshold is not the same for different data sets. After calculating velocity difference with sonic data over a short period of time, a number of 2.5 has been chosen for the three lidars in this study.

4.2 Lidar spectra with and without rain-suppressing normalization

It is important to point out that during the measurement time from 15:12 to 18:11 (UTC+1), lidar #2 was facing the wind almost all the time and we speculate that rainwater was covering the entrance window of the lidar telescope, despite our attempt to shield the window with a green rain barrel (Fig. 1). The water caused a very weak Doppler spectrum even at the minute with the highest rain intensity. Therefore, for further analysis and comparison, only the measurement data by lidar #1 and #3 are used.

It is worth noting that the wind direction at the minute with the highest rain intensity (15:48, UTC+1) is from $160°$ by the 10-minute averaged sonic data, and the two lidars' geographic beam directions are $42.6°$ and $299.3°$ (Fig. 2). Therefore, the wind is moving away from both lidars' laser beams at this minute, causing negative line-of-sight velocity. Consequently, the projection of the resultant velocity of raindrops, in the measuring configuration used here, is smaller than that of the horizontal
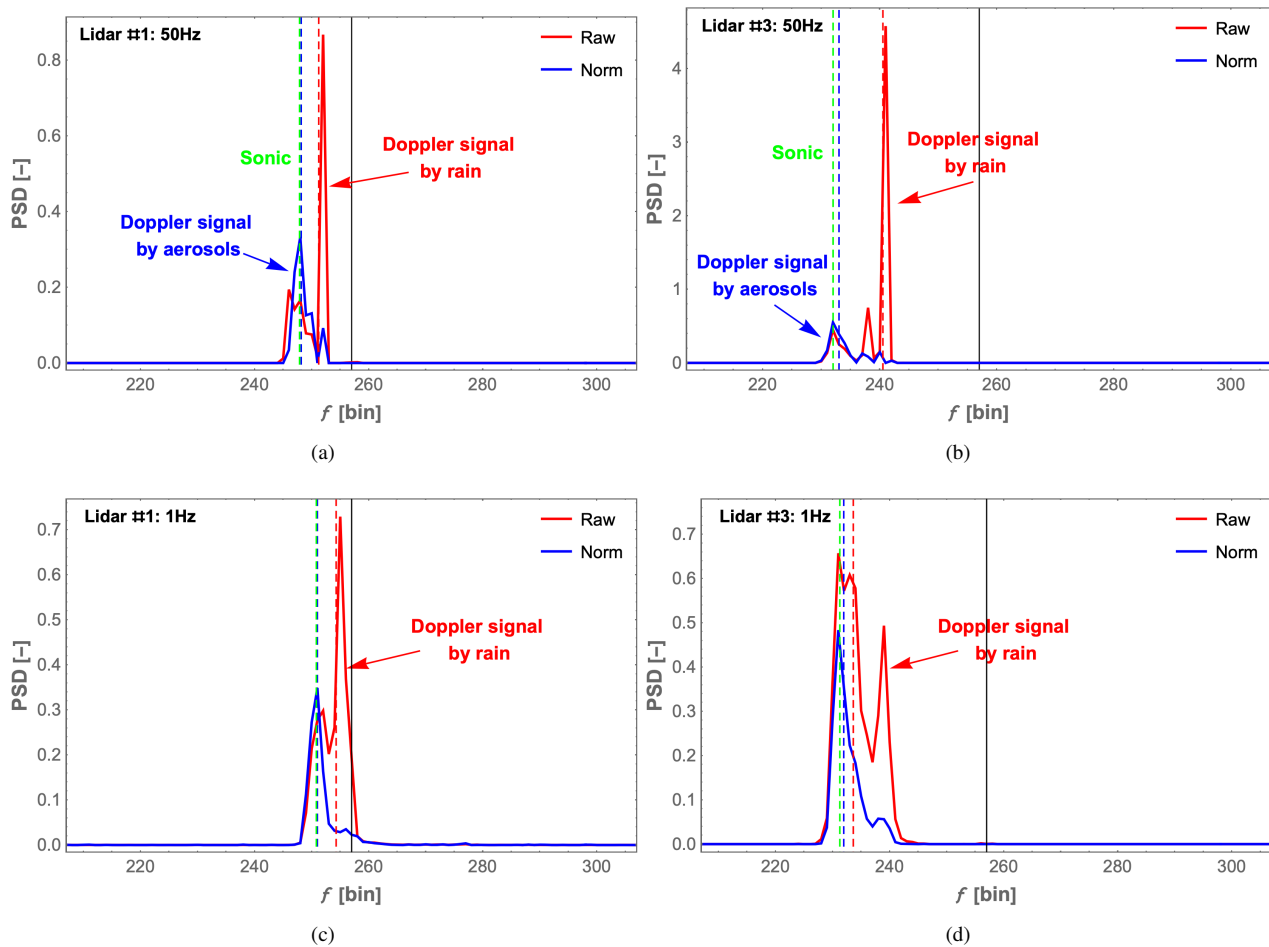
Figure 10. Comparison of Doppler spectra containing both wind and rain Doppler signals, with (marked by "Norm" short for normalization) and without (marked by "Raw") suppressing rain signals for two lidars at the moderate-rain minute (15:48, UTC+1). **(a)** and **(b)** 50-Hz-sampled spectra for lidar #1 and #3. **(c)** and **(d)** 1-Hz-sampled spectra for lidar #1 and #3. The red and blue dashed lines represent the median frequency bin of the raw and the normalized Doppler spectra, which are used to derive line-of-sight wind velocity. The green dashed line indicates the sonic wind velocity and the solid black line stands for the zero-Doppler shift at frequency bin 257.

220 wind speed in the beam direction. In Fig. 10, it is very obvious that after normalization by the spectral peak, the narrow Doppler signal caused by the raindrops (red arrows) is effectively suppressed and the bias between the reference sonic wind velocity and that of the lidars is reduced as can also be seen in Table 3, for example, from -1.56 to -0.18 ms^{-1} at 50 Hz for lidar #3. This indicates that normalization by the spectral peak value can help to reduce the influence of the raindrops since the narrow peak closer to the center zero frequency (the solid black line at frequency bin 257) is strongly suppressed.

225   In the section below, we compare the radial wind velocity detected by lidars and the sonic anemometer at 31 m height in detail in light of the promising results about the effective suppression of rain Doppler signals at one moderate-rain minute

Table 3. The estimated wind velocity by lidar data with (V_{norm}) and without (V_{raw}) normalization, and by the sonic anemometer (V_{sonic}) from 50 Hz and 1 Hz spectra at the moderate-rain minute (15:48, UTC+1).

	V_{sonic} (ms^{-1})	V_{raw} (ms^{-1})	V_{norm} (ms^{-1})
50 Hz of #1	-1.67	-1.06	-1.62
50 Hz of #3	-4.58	-3.02	-4.40
1 Hz of #1	-1.14	-0.50	-1.10
1 Hz of #3	-4.72	-4.29	-4.59

(15:48, UTC+1). The outcomes are elaborated to verify this rain-suppressing normalization method under no-rain, light-rain, and moderate-rain conditions.

5   Comparison between lidar and sonic wind velocity

5.1   50Hz wind velocity comparison

The reference 50 Hz sonic data at 31 m height was synchronized with the lidar measurements before the comparison. In Fig. 11, the 50 Hz radial wind velocity time series of the normalized lidar data (blue curves) matches well with the synchronized sonic data (green curves) at the no-rain, light-rain ($I_{rain} = 1$ mmh^{-1}) and moderate-rain ($I_{rain} = 4$ mmh^{-1}) minutes. It is very clear that the fluctuation of the wind velocity caused by the raindrops is effectively suppressed, especially during the moderate-rain period for lidar #1 with a shorter focus distance 37.2 m in Fig. 11e, or during the rainy period for lidar #3 with a longer focus distance 103.9 m in Fig. 11d and f. This can also be found from R^2 values, indicating less dispersion of the lidar wind velocity after rain-suppressing normalization.

Furthermore, Tables 4 and 5 compare the minute-averaged radial wind velocity of the three data sets (sonic, original raw lidar data without rain-suppressing normalization, and rain-suppressing normalized lidar data) as well as the bias between the sonic and lidar estimations. In the case of small probe lengths (lidar #1), only at the moderate-rain minute, the bias is effectively reduced from -0.15 to -0.04 ms^{-1} after normalization, whereas the bias is almost the same at the no-rain and light-rain minutes. However, precise wind velocity is obtained after normalization of lidar #3 data in the presence of light rain and moderate rain, with the bias correspondingly reduced from -0.21 to -0.01 ms^{-1} and from -0.33 to -0.08 ms^{-1}. In light of this, it follows that when the probe length is small and it rains more heavily than lightly, rain-suppressing normalization by the spectral peak value can suppress the rain signals effectively. However, when the probe length is larger (up to 10 m) with a broader Lorentzian weighting function, normalization performs very well when rain falls (whether light or heavy) because of the sensitivity of the lidar to rain signals.
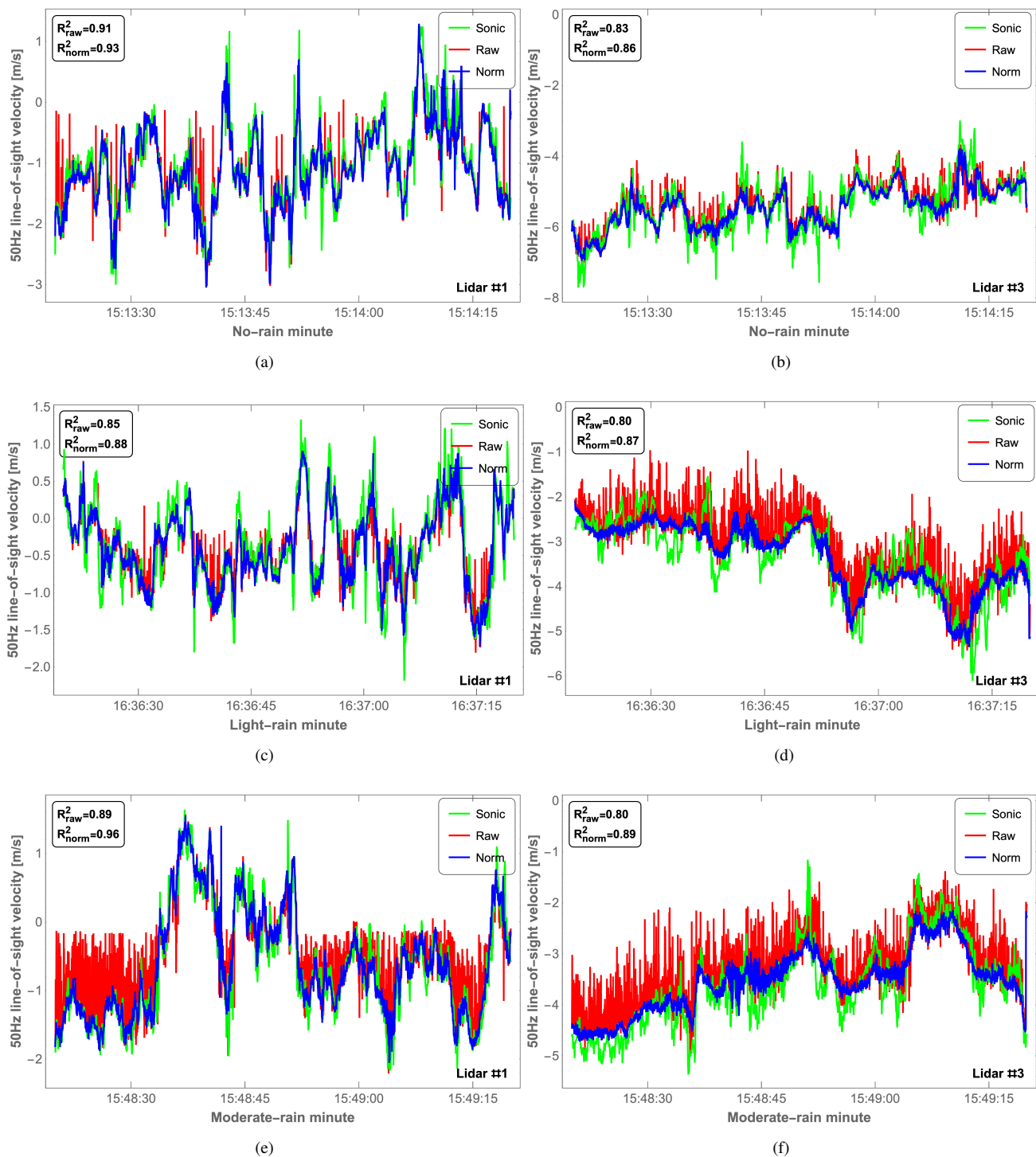
Figure 11. Comparison of 50 Hz radial wind measurements by sonic (green) and lidar (red and blue) at the no-rain, light-rain, and moderate-rain minutes from top to bottom. **(a)**, **(c)**, and **(e)** Lidar #1 (probe length of 1.2 m). **(b)**, **(d)**, and **(f)** lidar #3 (probe length of 9.8 m). The raw and normalized lidar data are marked in red and blue.

Table 4. 1-minute averaged wind velocity based on 50 Hz data and the corresponding bias between the sonic anemometer and lidar #1 (probe length of 1.2 m) at three minutes, with (norm) and without (raw) normalization. Rain intensity at the light-rain and moderate-rain minutes are 1 mmh^{-1} and 4 mmh^{-1}.

	V_{sonic} (ms^{-1})	V_{raw} (ms^{-1})	$V_{sonic} - V_{raw}$ (ms^{-1})	V_{norm} (ms^{-1})	$V_{sonic} - V_{norm}$ (ms^{-1})
No-rain minute 15:13:20+1min	-1.01	-1.07	0.06	-1.08	0.07
Light-rain minute 16:36:20+1min	-0.38	-0.39	0.01	-0.39	0.01
Moderate-rain minute 15:48:20+1min	-0.64	-0.49	-0.15	-0.60	-0.04

Table 5. 1-minute averaged wind velocity based on 50 Hz data and the corresponding bias between the sonic anemometer and lidar #3 (probe length of 9.8 m) at three minutes, with (norm) and without (raw) normalization. Rain intensity at the light-rain and moderate-rain minutes are 1 mmh^{-1} and 4 mmh^{-1}.

	V_{sonic} (ms^{-1})	V_{raw} (ms^{-1})	$V_{sonic} - V_{raw}$ (ms^{-1})	V_{norm} (ms^{-1})	$V_{sonic} - V_{norm}$ (ms^{-1})
No-rain minute 15:13:20+1min	-5.42	-5.41	-0.01	-5.45	0.03
Light-rain minute 16:36:20+1min	-3.37	-3.16	-0.21	-3.36	-0.01
Moderate-rain minute 15:48:20+1min	-3.62	-3.29	-0.33	-3.54	-0.08

In addition, the same conclusions can be drawn by comparing the probability density function (PDF) calculated for the radial wind velocity estimated based on the 1-minute averaged lidar spectra and the 50 Hz sonic data at three minutes, as shown in Fig. 12. The improvement by normalization for lidar #1 with a smaller probe length is observed only during the moderate rain period (Fig. 12e), as the calculated integral of the absolute difference of the PDF is reduced from 3.04 to 1.08 in Fig. 13. For lidar #3 with a larger probe length, normalization performs very well not only at the moderate-rain minute in Fig. 12f but also at the light-rain minute in Fig. 12d with the reduction of the integral of the absolute difference of the PDF from 1.68 to 0.57. In the comparison of the integral of the absolute difference of the PDF alone, normalization performs very well during rain periods when the probe length is large, or during moderate rain when the probe length is smaller, which is consistent with the conclusions discussed above.

At every minute, R^2 of lidar #3 is smaller than that of lidar #1 when comparing R^2 of the original raw lidar data in Fig. 11. We are uncertain about why rain seems to deteriorate the wind signal of lidar #3 more than that of lidar #1. It could have to do with the larger sample volume of #3 or the different elevation angles, but it could also have to do with a different amount of raindrops on the entrance windows of the telescope. The understanding of these sensitivities awaits more experimentation.
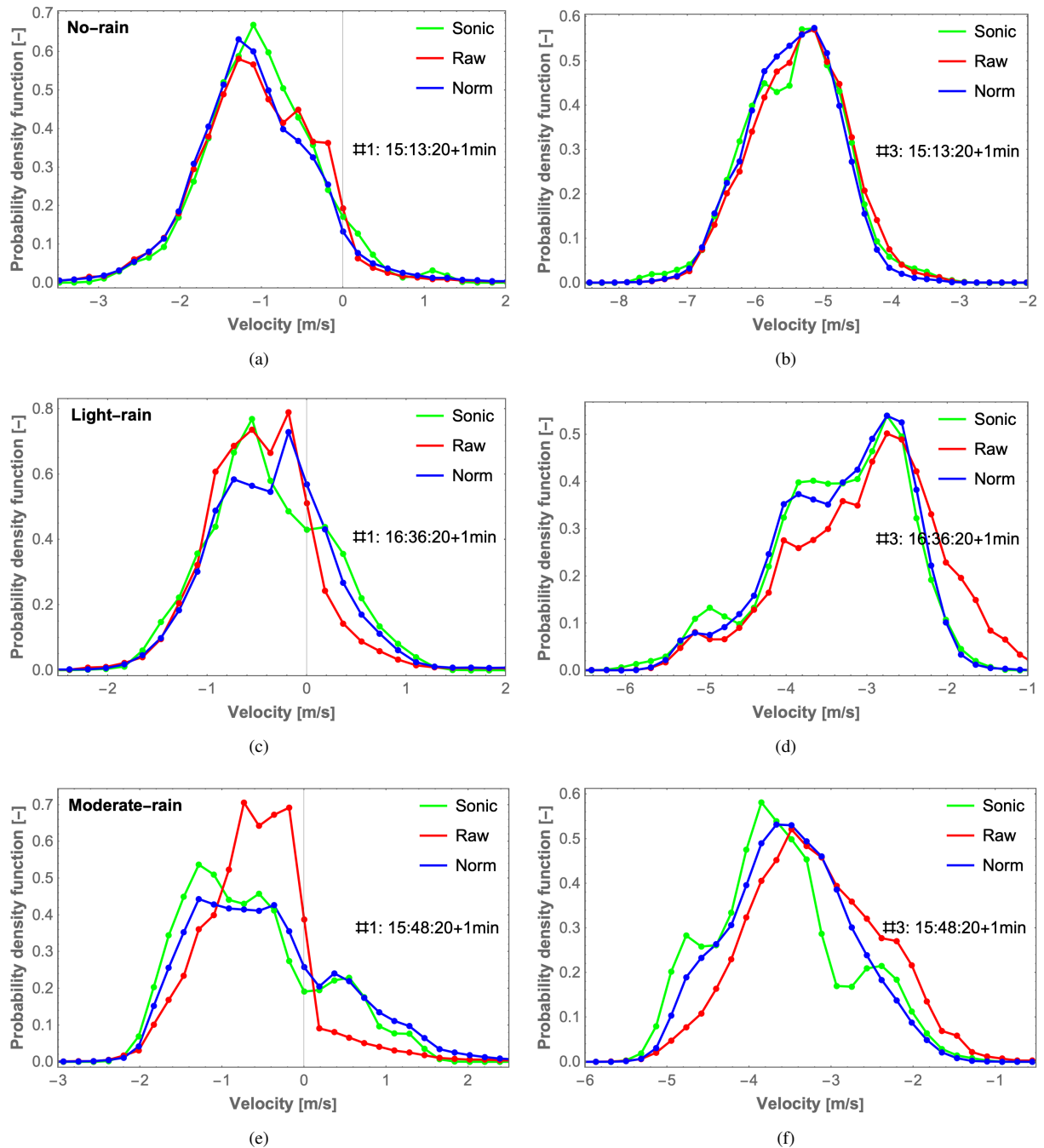
Figure 12. Probability density function (PDF) of radial wind velocity by 1-minute lidar spectra (red and blue) and 1-minute sonic data (green) at the no-rain (top row), light-rain (second row), and moderate-rain (bottom row) minutes. **(a)**, **(c)**, and **(e)** Lidar #1. **(b)**, **(d)**, and **(f)** Lidar #3. The raw and normalized lidar data are marked in red and blue.

(a)

(b)
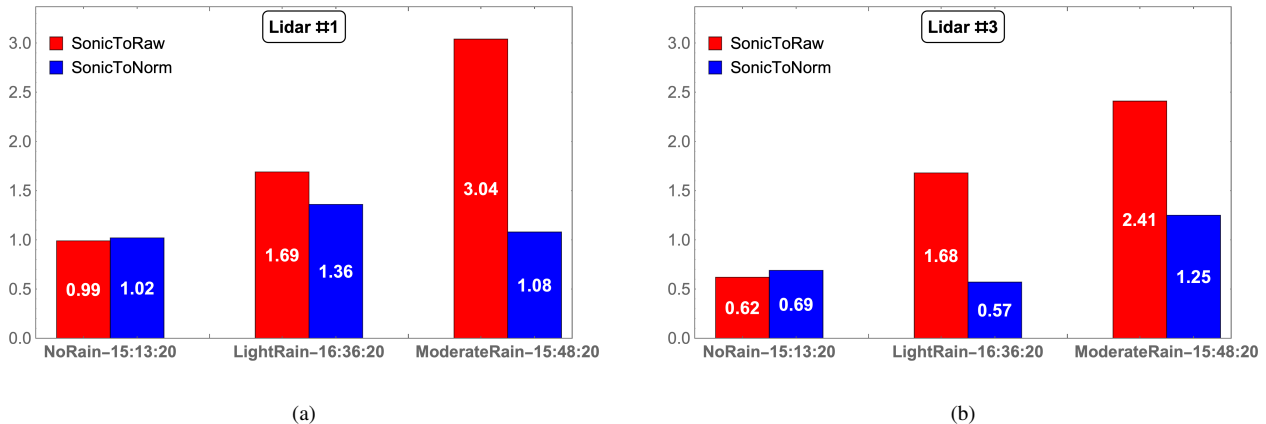
Figure 13. Comparison of the integral value of the PDF's absolute difference between the sonic and the lidar data with (SonicToNorm) and without (SonicToRaw) rain-suppressing normalization at no-rain, light-rain ($I_{rain} = 1$ mmh^{-1}), and moderate-rain ($I_{rain} = 4$ mmh^{-1}) minutes. **(a)** Lidar #1. **(b)** Lidar #3.

5.2   1-minute wind velocity comparison

The bias between the 1-minute sonic wind velocity and the lidar wind velocity, along with the rain intensity, are presented in Fig. 14. From the figure, we can draw similar conclusions as described previously. In the case of the lidar #1 with a smaller probe length in Fig. 14a, after normalization with the spectral peak, the large bias of the red curve around the rain intensity peak is effectively reduced from -0.15 to -0.03 ms^{-1}. This is a result of suppressing the low and negative velocities caused by raindrops. For other minutes, the estimated wind velocity after normalization is almost the same as the raw data, which aligns with the conclusions from 50 Hz data in Sect. 5.1.

For lidar #3, the improvement of wind velocity estimation by normalization is highly effective as presented in Fig. 14b, from when it started to rain at 15:29 until 16:48 (UTC+1). Afterward, at some minutes, the wind velocity time series after normalization overlaps with that of the raw lidar data, especially when the rain intensity is below 0.2 mmh^{-1} after 17:00. For most of the three-hour comparison period, the wind velocity calculated by the raw lidar data is underestimated, as shown in Fig. 14b. This is because of the small projection of the raindrop velocity, which counteracts the aerosol projection and adversely affects the estimated wind velocity. As well, the red curve shows a radial velocity difference of over 0.5 ms^{-1}.

In Fig. 15c, the 1-minute lidar wind velocity after the rain-suppressing normalization matches well with that of the sonic measurement for lidar #3 with a larger probe length, as the normalized lidar data (blue dots) are in a closer agreement with the sonic measurements compared with the raw lidar data (red dots). For lidar #1 in Fig. 15a, there is no obvious improvement after normalization by the spectral peak. However, the averaged bias in Fig. 15b and d demonstrate the performance of rain-suppressing normalization. It is clearly indicated by the red and blue fitted curves that the suppression becomes effective not only for lidar #3 when it rains, but also for lidar #1 with a short focus distance when the rain intensity is large. Due to the
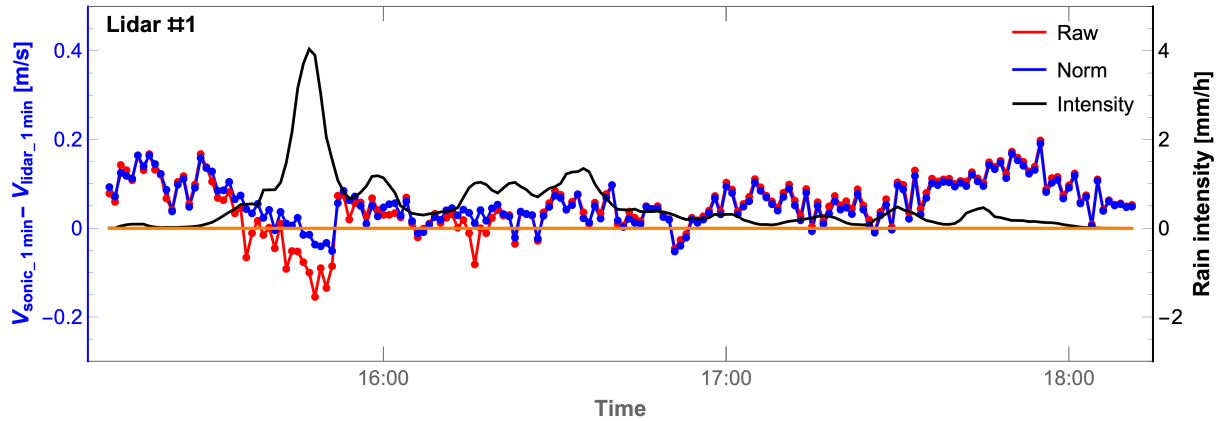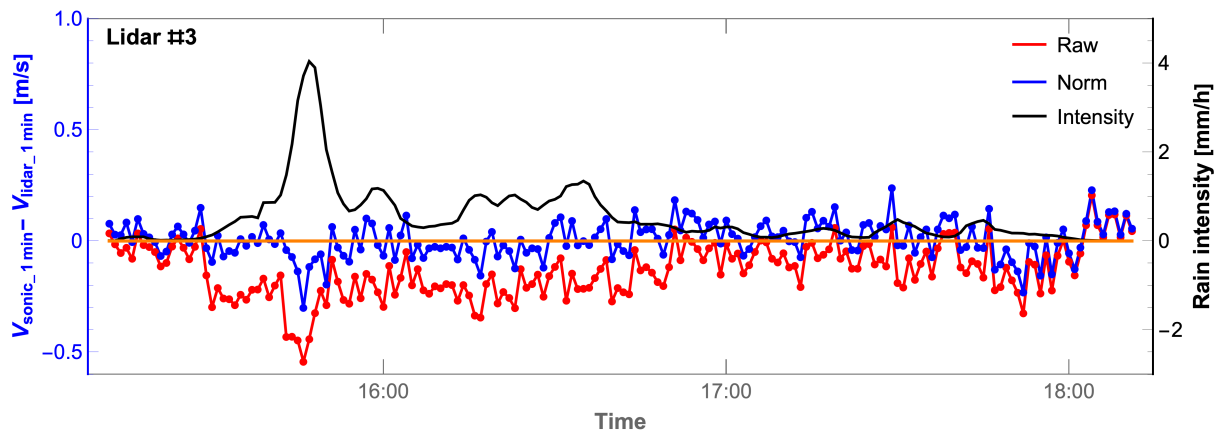
Figure 14. Difference of 1-minute averaged wind velocity between lidar and sonic measurements together with the rain intensity (the solid black curve) from 15:12 to 18:11 (UTC+1). **(a)** Lidar #1 with the probe length of 1.2 m. **(b)** Lidar #3 with the probe length of 9.8 m. The raw and normalized lidar data are marked in red and blue.
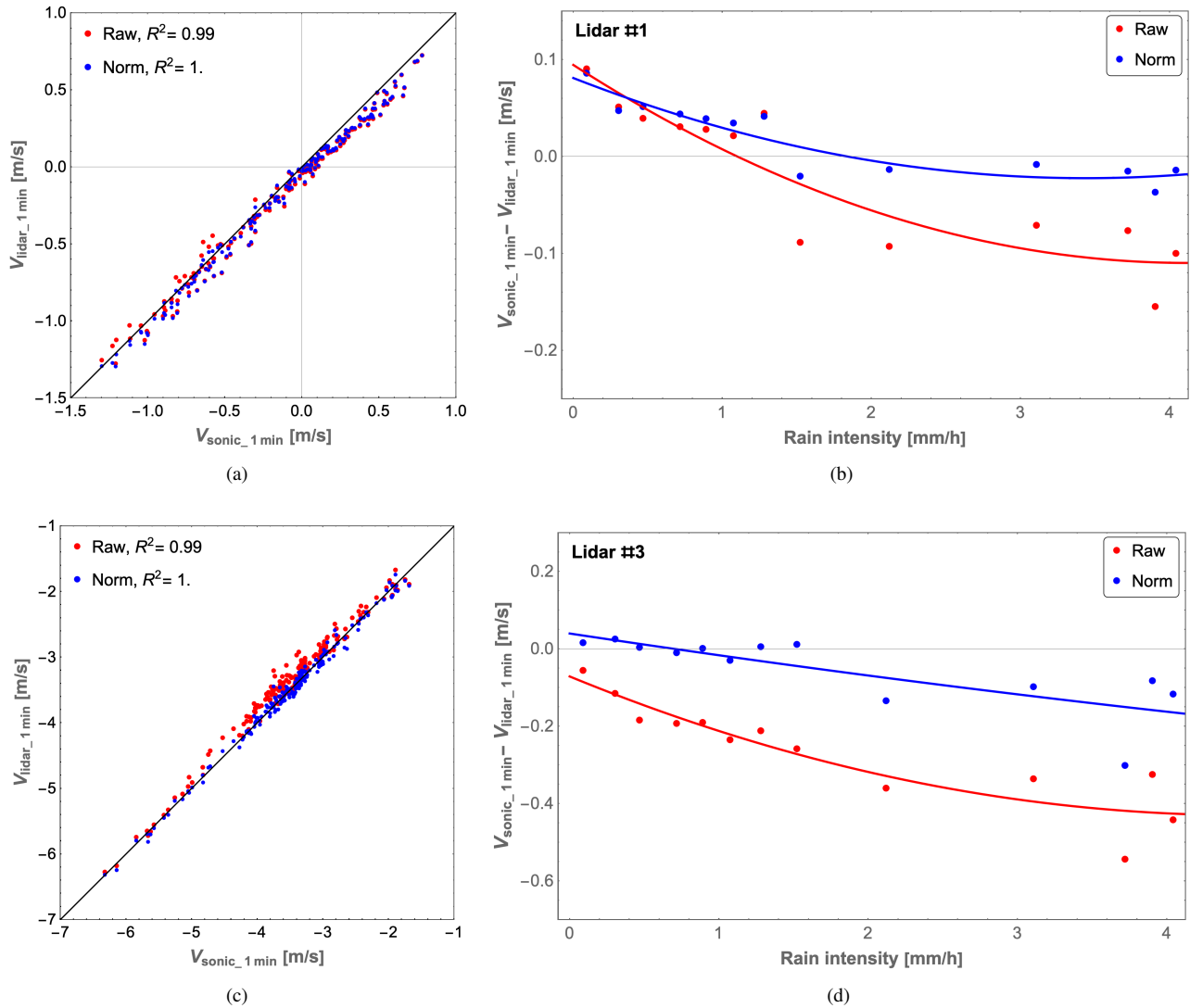
Figure 15. 1-minute wind velocity comparison between the lidar and sonic measurements from 15:12 to 18:11 (UTC+1) for lidar #1 (top row) and #3 (bottom row). **(a)** and **(c)** Scatter plot of 1-minute wind velocity. **(b)** and **(d)**) Averaged bias and its fitted function as a function of the rain intensity. The raw and normalized lidar data are marked in red and blue.

280   rare occurrence of raindrops passing through the laser beam with a condensed probe length, this method does not have a large impact on velocity determinations by lidar #1 during light rain, since at moderate rain there are only 0.05 raindrops remaining in the probe volume. These lead to the same conclusions discussed previously that rain-suppressing normalization performs well for the large probe length when it rains as well as for the small probe length when it rains more heavily than lightly.

6 Conclusions

285 In this paper, we have shown an experimental proof-of-concept demonstration of a method to reduce the bias caused by precipitation on continuous-wave Doppler lidar measurements of wind speed. This is accomplished by sampling Doppler spectra faster than most raindrops' beam transit time, which in the current case was at 3 kHz. Subsequently, the 3 kHz spectra are normalized with their peak values to suppress strong backscatter signals from raindrops before being averaged down to 50 Hz from which the radial wind velocity is determined.

290 Results from lidar beams with different elevation angles and focus distances were studied under different rain intensities measured by a disdrometer. The derived wind velocities were compared with a sonic anemometer reference. From the comparison, we find that the rain-suppressing normalization has the most significant impact on reducing bias when the probe volume (growing with the fourth power of the focus distance) is the largest. However, when the probe volume is small (shorter focus distances), the impact of rain is limited. Rain-induced bias also varies according to elevation angle but to a lesser extent.

295 However, the exact nature of these relations remains to be further verified and understood.

The tendency is that the more it rains, the stronger the bias and the more the rain-suppressing normalization reduces the bias. For moderate rain intensity (we do not have a heavy rain period in our data), the range of the bias is reduced from the interval 0.1 to $0.4 \, \mathrm{ms}^{-1}$ to 0.0 to $0.1 \, \mathrm{ms}^{-1}$. The suggested method in this study could also be investigated for rain events (containing heavy rain) on several days and also for pulsed Doppler lidars even though their measurement volume is quite larger than that

300 of the continuous-wave lidars. Further investigations could also attempt to retrieve the falling velocity and the size distribution of raindrops using the fast Doppler spectra.

Data availability. Data underlying the results presented in this paper can be obtained from the authors upon reasonable request.

Author contributions. All authors have made a contribution to the paper preparation. Conceptualization, JM, LJ, NA, MS; methodology, project management, and experiment conduction, LJ, NA, JM, MS; data analysis, LJ, JM; writing—original draft preparation, LJ; writ-

305 ing—review and editing, LJ, NA, JM, MS. All authors have read and agreed to the published version of the manuscript.

Competing interests. The authors declare no conflict of interest.

Acknowledgements. The authors are grateful to senior scientist Gunner Chr. Larsen (DTU) for his continued support and inspiration for the project. The authors would also like to thank Michael Courtney, Ebba Dellwik, Per Hansen, Karen Enevoldsen, Lars Christensen, Michael Rasmussen, and Claus Brian Munk Pedersen from DTU, for their helpful support during the field experiment, fruitful discussions, and helpful

310 comments.

Financial support. This research is mainly funded by the Innovation Training Network Marie Skłodowska-Curie Actions LIKE (LIdar Knowledge Europe) project and the LICOREIM (LIdar-assisted COntrol for REliability IMprovement) project. The LIKE project (H2020-MSCA-ITN-2019, Grant number 858358) is funded by the European Union. The LICOREIM project (Grant number 64019-0580) is funded by the Energy Technology Development and Demonstration Program (EUDP).

315   *Review statement.* This paper was edited by and reviewed by two anonymous referees.

References

Abari, C. F., Pedersen, A. T., and Mann, J.: An all-fiber image-reject homodyne coherent Doppler wind lidar, Optics express, 22, 25 880–25 894, 2014.

Angelou, N., Abari, F. F., Mann, J., Mikkelsen, T., and Sjöholm, M.: Challenges in noise removal from Doppler spectra acquired by a continuous-wave lidar, in: Proceedings of the 26th International Laser Radar Conference, Porto Heli, Greece, pp. 25–29, 2012a.

Angelou, N., Mann, J., Sjöholm, M., and Courtney, M.: Direct measurement of the spectral transfer function of a laser based anemometer, Review of scientific instruments, 83, 033 111, 2012b.

Angelou, N., Mann, J., and Dellwik, E.: Wind lidars reveal turbulence transport mechanism in the wake of a tree, Atmospheric Chemistry and Physics, 22, 2255–2268, 2022.

Angulo-Martínez, M., Beguería, S., Latorre, B., and Fernández-Raga, M.: Comparison of precipitation measurements by OTT Parsivel 2 and Thies LPM optical disdrometers, Hydrology and Earth System Sciences, 22, 2811–2837, 2018.

Aoki, M., Iwai, H., Nakagawa, K., Ishii, S., and Mizutani, K.: Measurements of rainfall velocity and raindrop size distribution using coherent Doppler lidar, Journal of Atmospheric and Oceanic Technology, 33, 1949–1966, 2016.

Bingöl, F., Mann, J., and Foussekis, D.: Conically scanning lidar error in complex terrain, Meteorologische Zeitschrift, pp. 189–195, 2009.

Bos, R., Giyanani, A., and Bierbooms, W.: Assessing the severity of wind gusts with lidar, Remote Sensing, 8, 758, 2016.

Bossanyi, E., Kumar, A., and Hugues-Salas, O.: Wind turbine control applications of turbine-mounted LIDAR, in: Journal of Physics: Conference Series, vol. 555, p. 012011, IOP Publishing, 2014.

Branlard, E., Pedersen, A. T., Mann, J., Angelou, N., Fischer, A., Mikkelsen, T., Harris, M., Slinger, C., and Montes, B.: Retrieving wind statistics from average spectrum of continuous-wave lidar, Atmospheric Measurement Techniques, 6, 1673–1683, 2013.

Brinkmeyer, E.: CW lidar for wind sensing featuring numerical range scanning and strong inherent suppression of disturbing reflections, in: Lidar Technologies, Techniques, and Measurements for Atmospheric Remote Sensing XI, vol. 9645, pp. 63–68, SPIE, 2015.

Cheynet, E., Jakobsen, J. B., Snæbjörnsson, J., Mikkelsen, T., Sjöholm, M., Mann, J., Hansen, P., Angelou, N., and Svardal, B.: Application of short-range dual-Doppler lidars to evaluate the coherence of turbulence, Experiments in Fluids, 57, 1–17, 2016.

Clima, T: Laser Precipitation Monitor Instruction for Use: 5.4110, https://www.thiesclima.com/db/dnl/5.4110.xx.x00_Laser_Precipitation_Monitor_eng.pdf, last access: 2 June 2023.

Davoust, S., Jehu, A., Bouillet, M., Bardon, M., Vercherin, B., Scholbrock, A., Fleming, P., and Wright, A.: Assessment and optimization of lidar measurement availability for wind turbine control, Tech. rep., National Renewable Energy Lab.(NREL), Golden, CO (United States), 2014.

Debnath, M., Iungo, G. V., Ashton, R., Brewer, W. A., Choukulkar, A., Delgado, R., Lundquist, J. K., Shaw, W. J., Wilczak, J. M., and Wolfe, D.: Vertical profiles of the 3-D wind velocity retrieved from multiple wind lidars performing triple range-height-indicator scans, Atmospheric Measurement Techniques, 10, 431–444, 2017.

Elshafei, B., Peña, A., Xu, D., Ren, J., Badger, J., Pimenta, F. M., Giddings, D., and Mao, X.: A hybrid solution for offshore wind resource assessment from limited onshore measurements, Applied Energy, 298, 117 245, 2021.

Glossary of Meteorology (June 2000): Rain, https://glossary.ametsoc.org/wiki/Rain, last access: 21 June 2023.

Gottschall, J., Papetta, A., Kassem, H., Meyer, P. J., Schrempf, L., Wetzel, C., and Becker, J.: Advancing Wind Resource Assessment in Complex Terrain with Scanning Lidar Measurements, Energies, 14, 3280, 2021.

Guo, F., Mann, J., Peña, A., Schlipf, D., and Cheng, P. W.: The space-time structure of turbulence for lidar-assisted wind turbine control, Renewable Energy, 2022.

Harris, M., Pearson, G. N., Ridley, K. D., Karlsson, C. J., Olsson, F. Å., and Letalick, D.: Single-particle laser Doppler anemometry at 1.55 µm, Applied Optics, 40, 969–973, 2001.

Held, D. P. and Mann, J.: Comparison of methods to derive radial wind speed from a continuous-wave coherent lidar Doppler spectrum, Atmospheric Measurement Techniques, 11, 6339–6350, 2018.

Henderson, S. W., Hale, C. P., Magee, J. R., Kavaya, M. J., and Huffaker, A. V.: Eye-safe coherent laser radar system at 2.1 µm using Tm, Ho: YAG lasers, Optics letters, 16, 773–775, 1991.

Izumi, Y. and Barad, M. L.: Wind speeds as measured by cup and sonic anemometers and influenced by tower structure, Journal of Applied Meteorology and Climatology, 9, 851–856, 1970.

Jena, D. and Rajendran, S.: A review of estimation of effective wind speed based control of wind turbines, Renewable and Sustainable Energy Reviews, 43, 1046–1062, 2015.

Jin, L., Angelou, N., Mann, J., and Larsen, G. C.: Improved wind speed estimation and rain quantification with continuous-wave wind lidar, in: Journal of Physics: Conference Series, vol. 2265, p. 022093, IOP Publishing, 2022.

Leica Geosystems: Introduction of Leica Total Station, https://leica-geosystems.com/products/total-stations, last access: 12 March 2023.

Li, J., Wang, X., and Yu, X. B.: Use of spatio-temporal calibrated wind shear model to improve accuracy of wind resource assessment, Applied energy, 213, 469–485, 2018.

Mann, J., Angelou, N., Arnqvist, J., Callies, D., Cantero, E., Arroyo, R. C., Courtney, M., Cuxart, J., Dellwik, E., Gottschall, J., et al.: Complex terrain experiments in the new european wind atlas, Philosophical Transactions of the Royal Society A: Mathematical, Physical and Engineering Sciences, 375, 20160 101, 2017.

Menke, R., Vasiljević, N., Wagner, J., Oncley, S. P., and Mann, J.: Multi-lidar wind resource mapping in complex terrain, Wind Energy Science, 5, 1059–1073, 2020.

Mikkelsen, T., Mann, J., Courtney, M., and Sjöholm, M.: Windscanner: 3-D wind and turbulence measurements from three steerable Doppler lidars, in: IOP conference series: earth and environmental science, vol. 1, p. 012018, IOP Publishing, 2008.

Mikkelsen, T., Angelou, N., Hansen, K., Sjöholm, M., Harris, M., Slinger, C., Hadley, P., Scullion, R., Ellis, G., and Vives, G.: A spinner-integrated wind lidar for enhanced wind turbine control, Wind Energy, 16, 625–643, 2013.

Mikkelsen, T., Sjöholm, M., Angelou, N., and Mann, J.: 3D WindScanner lidar measurements of wind and turbulence around wind turbines, buildings and bridges, in: IOP Conference Series: Materials Science and Engineering, vol. 276, p. 012004, IOP Publishing, 2017.

Mikkelsen, T., Sjöholm, M., Astrup, P., Peña, A., Larsen, G., Van Dooren, M., and Sekar, A. K.: Lidar Scanning of Induction Zone Wind Fields over Sloping Terrain, in: Journal of Physics: Conference Series, vol. 1452, p. 012081, IOP Publishing, 2020.

Peña, A., Hasager, C. B., Gryning, S.-E., Courtney, M., Antoniou, I., and Mikkelsen, T.: Offshore wind profiling using light detection and ranging measurements, Wind Energy: An International Journal for Progress and Applications in Wind Power Conversion Technology, 12, 105–124, 2009.

Peña, A., Hasager, C., Badger, M., Barthelmie, R., Bingöl, F., Cariou, J.-P., Emeis, S., Frandsen, S., Harris, M., Karagali, I., Larsen, S., Mann, J., Mikkelsen, T., Pitter, M., Pryor, S., Sathe, A., Schlipf, D., Slinger, C., and Wagner, R.: Remote Sensing for Wind Energy, no. 0084(EN) in DTU Wind Energy E, DTU Wind Energy, Denmark, 2015.

Press, W. H., Vetterling, W. T., Teukolsky, S. A., and Flannery, B. P.: Numerical recipes, Citeseer, 1988.

Samadianfard, S., Hashemi, S., Kargar, K., Izadyar, M., Mostafaeipour, A., Mosavi, A., Nabipour, N., and Shamshirband, S.: Wind speed prediction using a hybrid model of the multi-layer perceptron and whale optimization algorithm, Energy Reports, 6, 1147–1159, 2020.

Sathe, A. and Mann, J.: A review of turbulence measurements using ground-based wind lidars, Atmospheric Measurement Techniques, 6, 3147–3167, 2013.

Schlipf, D., Haizmann, F., Cosack, N., Siebers, T., and Cheng, P. W.: Detection of wind evolution and lidar trajectory optimization for lidar-assisted wind turbine control, 2015.

Sempreviva, A. M., Barthelmie, R. J., and Pryor, S.: Review of methodologies for offshore wind resource assessment in European seas, Surveys in Geophysics, 29, 471–497, 2008.

Sjöholm, M., Angelou, N., Hansen, P., Hansen, K. H., Mikkelsen, T., Haga, S., Silgjerd, J. A., and Starsmore, N.: Two-dimensional rotor-craft downwash flow field measurements by lidar-based wind scanners with agile beam steering, Journal of Atmospheric and Oceanic Technology, 31, 930–937, 2014.

Tilg, A.-M., Hasager, C., Veien, F., Badger, M., Rasmussen, M., Verhoef, J., and Skrzypinski, W.: Precipitation in the context of wind turbine blade erosion, 2020.

Träumner, K., Handwerker, J., Wieser, A., and Grenzhäuser, J.: A synergy approach to estimate properties of raindrop size distributions using a Doppler lidar and cloud radar, Journal of Atmospheric and Oceanic Technology, 27, 1095–1100, 2010.

Türk, M. and Emeis, S.: The dependence of offshore turbulence intensity on wind speed, Journal of Wind Engineering and Industrial Aero-dynamics, 98, 466–471, 2010.

Van Ulden, A. and Holtslag, A.: Estimation of atmospheric boundary layer parameters for diffusion applications, Journal of Applied Meteo-rology and Climatology, 24, 1196–1207, 1985.

Vasiljević, N., LM Palma, J. M., Angelou, N., Carlos Matos, J., Menke, R., Lea, G., Mann, J., Courtney, M., Frölen Ribeiro, L., and MGC Gomes, V. M.: Perdigão 2015: methodology for atmospheric multi-Doppler lidar experiments, Atmospheric Measurement Tech-niques, 10, 3463–3483, 2017.

Viselli, A., Filippelli, M., Pettigrew, N., Dagher, H., and Faessler, N.: Validation of the first LiDAR wind resource assessment buoy system offshore the Northeast United States, Wind Energy, 22, 1548–1562, 2019.

Wei, T., Xia, H., Hu, J., Wang, C., Shangguan, M., Wang, L., Jia, M., and Dou, X.: Simultaneous wind and rainfall detection by power spectrum analysis using a VAD scanning coherent Doppler lidar, Optics express, 27, 31 235–31 245, 2019.

Wei, T., Xia, H., Yue, B., Wu, Y., and Liu, Q.: Remote sensing of raindrop size distribution using the coherent Doppler lidar, Optics Express, 29, 17 246–17 257, 2021.

Wildmann, N., Päschke, E., Roiger, A., and Mallaun, C.: Towards improved turbulence estimation with Doppler wind lidar velocity-azimuth display (VAD) scans, Atmospheric Measurement Techniques, 13, 4141–4158, 2020.

Zhang, L. and Yang, Q.: A method for yaw error alignment of wind turbine based on LiDAR, IEEE Access, 8, 25 052–25 059, 2020.